

Article

Fatigue Behavior of Metastable Austenitic Stainless Steels in LCF, HCF and VHCF Regimes at Ambient and Elevated Temperatures [†]

Marek Smaga ^{1,*}, Annika Boemke ¹, Tobias Daniel ¹, Robert Skorupski ², Andreas Sorich ² and Tilmann Beck ¹

¹ Institute of Materials Science and Engineering, TU Kaiserslautern, 67663 Kaiserslautern, Germany; boemke@mv.uni-kl.de (A.B.); daniel@mv.uni-kl.de (T.D.); beck@mv.uni-kl.de (T.B.)

² Former employee of the Institute of Materials Science and Engineering, TU Kaiserslautern, 67663 Kaiserslautern, Germany; skorupski@mv.uni-kl.de (R.S.); sorich@mv.uni-kl.de (A.S.)

* Correspondence: smaga@mv.uni-kl.de; Tel.: +49-631-205-2762

[†] On the occasion of his 70th birthday, this work is dedicated to our mentor, colleague and friend Prof. Dr.-Ing. habil. Dietmar Eifler.

Received: 31 May 2019; Accepted: 19 June 2019; Published: 21 June 2019



Abstract: Corrosion resistance has been the main scope of the development in high-alloyed low carbon austenitic stainless steels. However, the chemical composition influences not only the passivity but also significantly affects their metastability and, consequently, the transformation as well as the cyclic deformation behavior. In technical applications, the austenitic stainless steels undergo fatigue in low cycle fatigue (LCF), high cycle fatigue (HCF), and very high cycle fatigue (VHCF) regime at room and elevated temperatures. In this context, the paper focuses on fatigue and transformation behavior at ambient temperature and 300 °C of two batches of metastable austenitic stainless steel AISI 347 in the whole fatigue regime from LCF to VHCF. Fatigue tests were performed on two types of testing machines: (i) servohydraulic and (ii) ultrasonic with frequencies: at (i) 0.01 Hz (LCF), 5 and 20 Hz (HCF) and 980 Hz (VHCF); and at (ii) with 20 kHz (VHCF). The results show the significant influence of chemical composition and temperature of deformation induced α' -martensite formation and cyclic deformation behavior. Furthermore, a “true” fatigue limit of investigated metastable austenitic stainless steel AISI 347 was identified including the VHCF regime at ambient temperature and elevated temperatures.

Keywords: austenitic stainless steel; metastability; LCF; HCF; VHCF; ambient and elevated temperatures

1. Introduction

In the early stages of the development of stainless steels, the passivity of the material and, therefore, its “stainlessness” was the main scope of development [1,2]. Chemical passivity of steels in many environmental conditions is achieved by alloying at least about 11 wt% chromium to the base material. Due to an excellent combination of mechanical and technological properties, as well as corrosion resistance, austenitic stainless steels are the most prevalent group of stainless steels—widely used for components in nuclear power and chemical plants as well as a great variety of industrial, architectural and biological applications [3–6]. Since the chromium contents of typical austenitic stainless steels exceed 16 wt%, their equilibrium microstructure at room temperature would be fully ferritic, if no other austenite stabilizing alloying elements were added to the material. Elements most often used to obtain an austenitic microstructure are nickel, manganese, carbon and nitrogen. Because carbon has a very high affinity with chromium, chromium carbides are prone to develop particularly at

high temperatures. This can reduce the chromium solid solution content in the austenitic matrix to less than 11 wt% and, consequently, lead to localized loss of stainlessness, especially at, or close to, the grain boundaries, resulting—under certain conditions—in intercrystalline corrosion. Therefore, in order to assure the corrosion resistivity of austenitic stainless steels, a very low carbon content and/or alloying with elements of a higher affinity with carbon, (e.g. niobium or titanium) are required [4]. In some cases, the ferromagnetic body centered cubic (bcc) δ -ferrite can be obtained in the paramagnetic face centered cubic (fcc) γ -austenitic microstructure directly after the manufacturing or melting process [7–10]. Indeed, δ -ferrite is a stable phase and its volume fraction does not change during mechanical loading. Generally, the influence of the chemical composition of Cr-Ni stainless steels on the initial microstructure at ambient temperature (AT) obtained after solution annealing heat treatment can be roughly estimated from the Cr and Ni content using the Maurer diagram [1]. Furthermore, the Schaeffler diagram provides more detailed information based on Cr and Ni equivalents taking other alloying elements besides Cr and Ni into account and is generally used for determining welding microstructures in Cr-Ni stainless steels [11].

The change in chemical composition not only influences the passivity of austenitic stainless steel but also significantly affects the metastability of austenite [12–16], meaning it is susceptible to undergoing phase transformations. Hence, the paramagnetic γ -austenite can transform by plastic deformation to a more stable microstructure, i.e. paramagnetic hexagonal close-packed (hcp) ϵ -martensite and/or body centered cubic (bcc) α' -martensite [17–24]. Scheil, one of the earliest researchers in this field, investigated the γ -austenite to α' -martensite transformation by measuring magnetic properties [25]. The change in magnetic properties by phase transformation can be used for non-destructive detection of α' -martensite as well as for monitoring fatigue processes in metastable austenites [26]. However, δ -ferrite, in the initial state of metastable austenite, has to be clearly separated from deformation-induced α' -martensite because both phases are ferromagnetic [7–10]. Deformation-induced phase transformations in metastable austenite affect significantly the fatigue process and are influenced by chemical composition [12–16], temperature [14,27–30] (encompassed by stacking fault energy (SFE) [31–39]), as well as grain size [32,40–43] strain amplitude [29,44–47] strain rate [48–50] and strain/stress state [51]. Additionally, SFE in fcc materials influences the slip character of dislocation, which has been summarized in the cyclic deformation map as a function of SFE and plastic strain amplitude given in [52–54]. For low SFE, independent of strain (stress) amplitude, the planar slip character occurs but for materials with higher SFE, a dependency of strain (stress) amplitude on dislocation slip character exists. High strain (stress) amplitude in the low cycle fatigue (LCF) regime leads to the development of the cell dislocation structure, which correlates with the wavy slip character of dislocation. The decrease of strain (stress) amplitude results in the formation of persistent slip bands in the high cycle fatigue (HCF) regime. Between the LCF and HCF regimes and lower and higher SFE, mixed dislocation structures can be observed [52–54]. A cyclic dislocation structure map of fcc materials with different SFE is not currently available for the very high cycle fatigue (VHCF) regime. The relationship between dislocation slip character and SFE described above was found for stable fcc materials [52–54]. In the case of metastable fcc austenite, SFE influences not only the dislocation slip character but also the deformation-induced phase transformation in ϵ and/or α' -martensite [17–24] as well as the formation of twins [55–57]. Figure 1 summarizes the microstructural changes in metastable austenitic Cr-Ni stainless steels due to cyclic mechanical loading, supported by TEM micrographs, which influence the cyclic deformation behavior of metastable austenitic stainless steels and consequently fatigue life. In this context, the present paper focuses on microstructural changes in metastable austenitic stainless steels, their cyclic deformation and transformation behavior at ambient and elevated temperatures in the whole fatigue regime from LCF to VHCF.

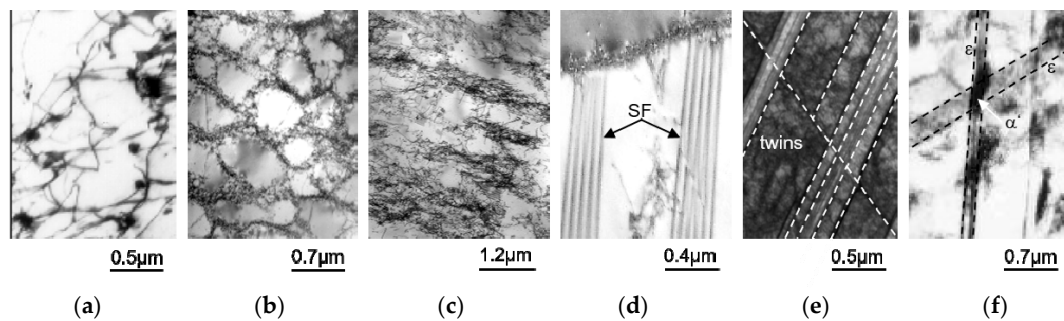


Figure 1. TEM micrographs with deformation and transformation microstructures of cyclically loaded metastable austenitic stainless steels: (a) typical dislocation density of the initial state after solution annealing, AISI 348 [58]; (b) cell dislocation structure (wavy slip character) at N_f in AISI 348 fatigued with $\sigma_a = 280$ MPa, $R = -1$ at AT with $f = 5$ Hz [58]; (c) dislocation accumulation in one direction (planar slip character) at N_f in AISI 348 fatigued with $\sigma_a = 260$ MPa, $R = -1$ at AT with $f = 5$ Hz [58]; (d) stacking faults (SF) at N_f in AISI 304 fatigued with $\varepsilon_{a,t} = 0.325\%$, $R = -1$ at AT with $f = 5$ Hz [58]; (e) twins in AISI 347 fatigued with $\sigma_a = 160$ MPa, $R = -1$ at $T = 300$ °C with $f = 980$ Hz at $N = 5 \times 10^8$, (f) ε - and α' -martensite at N_f in AISI 321 fatigued with $\sigma_a = 330$ MPa, $R = -1$ at AT with $f = 5$ Hz [59].

2. Materials

The investigated material was metastable austenitic stainless steel AISI 347 (X10CrNiNb1810, 1.4550) in two batches (A and B). The chemical composition of both batches is given in Table 1, which corresponds to German and international standards [60,61]. However, it is important to note that these standards do not take into consideration the metastability of the austenitic microstructure, but focus on the stainlessness of the steel. It is known that the same type of austenitic stainless steel can exist in significantly different states of metastability [16] up to a fully stable state. The material's metastability can be characterized by experimentally estimated equations, which describe the martensitic start (M_S) or deformation-induced transformation temperature (M_d) as well as the stacking fault energy (SFE), according to the chemical composition of austenitic stainless steels. In the literature, several equations for M_S [13], M_{d30} [14] and SFE [34] are given. Table 1 gives examples of these metastability parameters according to the following equations:

$$M_{d30,Angel} \text{ in } ^\circ\text{C} = 413 - 462 \cdot (C+N) - 13.7 \cdot Cr - 9.5 \cdot Ni - 8.1 \cdot Mn - 18.5 \cdot Mo - 9.2 \cdot Si \quad (1)$$

$$M_{S,Eichelmann} \text{ in } ^\circ\text{C} = 1350 - 1665 \cdot (C+N) - 42 \cdot Cr - 61 \cdot Ni - 33 \cdot Mn - 28 \cdot Si \quad (2)$$

$$\text{SFE in mJ/m}^2 = 25.7 + 2 \cdot Ni - 0.9 \cdot Cr - 1.2 \cdot Mn + 410 \cdot C - 77 \cdot N - 13 \cdot Si \quad (3)$$

The investigated austenitic stainless steel batches are in a metastable state (M_{d30} is in the range of ambient temperature). M_{d30} is the temperature at which 50 vol% of α' -martensite is developed by 30% of true plastic deformation [14] and was introduced for the comparison of the metastability of austenitic stainless steels. However, the deformation-induced phase transformation from γ -austenite into α' -martensite can also take place at higher temperatures than M_{d30} [46,58,59,62,63]. The amount of deformation induced α' -martensite depends: (i) on the initial conditions, given by production process, such as chemical composition and initial microstructure e.g. the grain size of austenite, dislocation arrangements/density, precipitations and (ii) on loading parameters, like deformation temperature, amount of plastic deformation, as well as the stress and strain state/rate. Therefore, determining the true M_d -temperature above which no α' -martensite formation takes place is not practically possible. In order to take into account both aspects specified above (i and ii) on the susceptibility of forming α' -martensite in metastable austenite, a method based on dynamically applied local plastic deformation and magnetic measurement was developed [16]. The parameter established by this method as I_ξ correlates very well with the grade of α' -martensite formation during cyclic loading and allows to distinguish the susceptibility of austenitic stainless steels, which have the same chemical composition

and grain size, to undergo phase transformation. The I_{ξ} parameter of the two investigated batches of AISI 347 is given in Table 1. Table 2 summarizes the mechanical properties of the investigated material at ambient temperature (AT) and $T = 300\text{ }^{\circ}\text{C}$ as well as α' -martensite content after specimen failure.

Table 1. Chemical composition in weight % and metastability parameters.

AISI 347	C	N	Nb	Cr	Ni	Mn	Mo	Si	$M_{d30}\text{ }^{\circ}\text{C}$	$M_S\text{ }^{\circ}\text{C}$	SFE mJ/m^2	I_{ξ} FE%
Batch A	0.040	0.007	0.62	17.6	10.6	1.83	0.29	0.41	25	−189	39	0.25
Batch B	0.024	0.019	0.41	17.3	9.3	1.55	0.19	0.63	46	−81	27	0.66

Table 2. Mechanical properties and α' -martensite content after specimen failure (ξ).

AISI 347	$R_{p0.2}$ in MPa	UTS in MPa	A in %	ξ in FE%
Batch A, AT	242	569	66	4.41
Batch A, 300 $^{\circ}\text{C}$	180	357	36	0.00
Batch B, AT	220	621	51	33.22
Batch B, 300 $^{\circ}\text{C}$	155	428	37	0.00

Shown in Figure 2 are light and electron microscopy micrographs of longitudinal sections of the initial microstructure of the investigated materials in the solution-annealed state and after plastic deformation. Specimens from batch A were extracted from an original nuclear power plant surge line pipe with an outside diameter of 333 mm and a wall thickness of 36 mm. The pipe was manufactured seamless, drilled from the inside, turned from the outside and delivered in a solution-annealed state (1050 $^{\circ}\text{C}$ / 10 min / H_2O), such that in the initial state no α' -martensite was detected. Note that the surge line pipe was investigated in the as-manufactured condition and has not been previously used in a nuclear power plant. The material of batch B was provided as rolled bars with a diameter of 25 mm in a solution-annealed state. A fully austenitic microstructure was obtained by additional annealing at 1050 $^{\circ}\text{C}$ for 35 minutes and quenching in helium atmosphere.

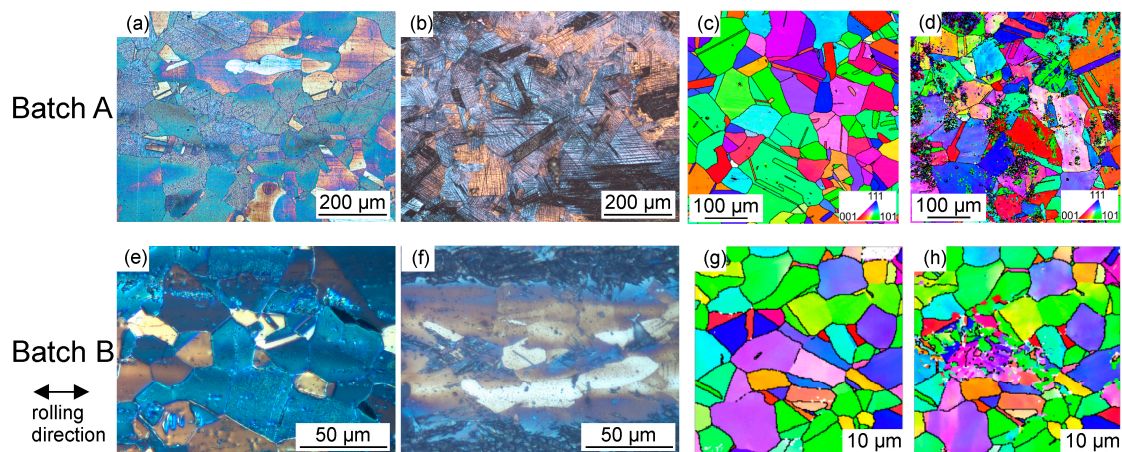


Figure 2. Optical micrographs of longitudinal sections using Bloech & Wedl I etching (a,e) initial state, (b,f) after plastic deformation as well as EBSD grain maps of (c,g) initial state and (d,h) after plastic deformation.

In Figure 2a the optical micrograph of the initial state of batch A is shown. This micrograph was taken after color etching using a Bloech & Wedl I etching agent, which is able to visualize local inhomogeneities in chemical composition [15]. A homogeneous distribution of the Cr and Ni content was detected in the microstructures of batch A. Furthermore, plastic deformation of batch A led to the homogeneous development of α' -martensite in the austenite matrix during plastic deformation (see Figure 2b,d). An electron backscatter diffraction (EBSD) micrograph of the initial state

of both batches (Figure 2c,g) revealed a one-phase microstructure with annealing twins, typical for austenitic stainless steels. The same etching and observation techniques were used for characterizing the microstructure of batch B. In the case of batch B, the etching agent revealed local chemical inhomogeneities caused by slight variations of the Cr and Ni content as blue and brown bands (Figure 2e), which could not be removed during solution annealing. The blue band correlates with a lower Ni and higher Cr content, while the brown bands indicate higher Ni and lower Cr contents [15]. The band structure with a corresponding local metastability of austenitic microstructure led to a pronounced α' -martensite formation in regions with higher Cr content (Figure 2f). The local chemically induced band structure could not be observed in scanning electron micrographs using EBSD technique (Figure 2h). Instead, the EBSD image shows a homogeneous crystallographic microstructure in both cases, whereas the deformation-induced α' -martensite formation after plastic deformation can be clearly detected by EBSD images (Figure 2d,h). The comparison of EBSD grain maps (Figure 2c,g) of both batches presented a clear difference in the grain size. Quantitative evaluation yielded a mean grain size of 120 μm for batch A and of 17 μm for batch B, respectively.

3. Methods

To investigate the fatigue behavior of metastable austenitic stainless steels at ambient and elevated temperatures from the LCF to VHCF regime, servohydraulic and ultrasonic fatigue systems were used. The test temperature of $T = 300\text{ }^{\circ}\text{C}$ was achieved using an inductive heating system and control based on measurement by a type-K ribbon thermocouple in the center of the gauge length. The isothermal LCF and HCF tests at ambient temperature (AT) and $T = 300\text{ }^{\circ}\text{C}$ were performed with an MTS 100 kN servohydraulic testing system using load frequency of $f = 0.01\text{ Hz}$ (LCF), 5 Hz and 20 Hz (HCF), see Figure 3a and b. The VHCF tests at $T = 300\text{ }^{\circ}\text{C}$ were performed with $f = 980\text{ Hz}$ at an MTS 1 kHz servohydraulic testing system (Figure 3c). The VHCF tests at AT were realized in an ultrasonic fatigue testing system developed and built up at the authors' institute [64,65] (Figure 3d) with an operating frequency $f = 20\text{ kHz}$. In order to characterize the cyclic deformation behavior in the LCF and HCF regime, respectively, an extensometer (AT and $T = 300\text{ }^{\circ}\text{C}$) and thermocouples (only AT) were used. The area of each hysteresis loop describes the cyclic plastic strain energy dissipated per unit volume during a given loading cycle, which is mainly dissipated into heat and, hence, results in a change in specimen temperature [66,67]. Temperature was measured with one thermocouple in the middle of the gauge length (T_1) and two reference thermocouples at the elastically loaded specimen shafts (T_2 , T_3). The temperature change induced by cyclic plastic deformation was calculated according to:

$$\Delta T = T_1 - 0.5 \cdot (T_2 + T_3) \quad (4)$$

The in situ detection of fatigue induced α' -martensite formation was done by magnetic FeritscopeTM (FISCHER, Windsor, CT, USA) measurements at AT (see Figure 3a). Due to the higher permeability of ferromagnetic ferrite compared to paramagnetic austenite, the response of the material to magnetic induction increases with the ferrite content. Using a non-destructive magnetic method, the FeritscopeTM measures the relative permeability of a material in the alternating magnetic field of its probe. This provides a ferrite content signal (FE%), which is also influenced by the curvature of the specimen's surface and stress-strain state. Furthermore, to determine the ferromagnetic α' -martensite content in vol%, the FeritscopeTM signal (FE%) needs to be multiplied by a factor of 1.7 [68]. Because the calibration factor was determined only for α' -martensite contents below 55 FE%, in the following diagrams the magnetically determined α' -martensite is indicated as ξ in FE% without calculating the vol% of α' -martensite. Furthermore, within one load cycle, the magnetic properties of α' -martensite are influenced by stress/strain due to the Villari effect (inverse magnetostriction), which describes a change of the magnetic susceptibility of ferromagnetic material due to mechanical stresses [26]. Therefore, an arithmetic mean value per load cycle of the measured FeritscopeTM signal is given in the diagrams. For specimens loaded in LCF, HCF and VHCF tests at $T = 300\text{ }^{\circ}\text{C}$ and in VHCF tests at AT, ex situ

Feritscope™ measurements were performed. The fatigue tests at AT and $T = 300\text{ °C}$ were total strain controlled in LCF regime and stress controlled in the HCF regime. The VHCF tests at $T = 300\text{ °C}$ were stress controlled and the ultrasonic VHCF tests at AT performed in displacement-control. All tests were performed in symmetric push-pull conditions with load ratio $R = -1$.

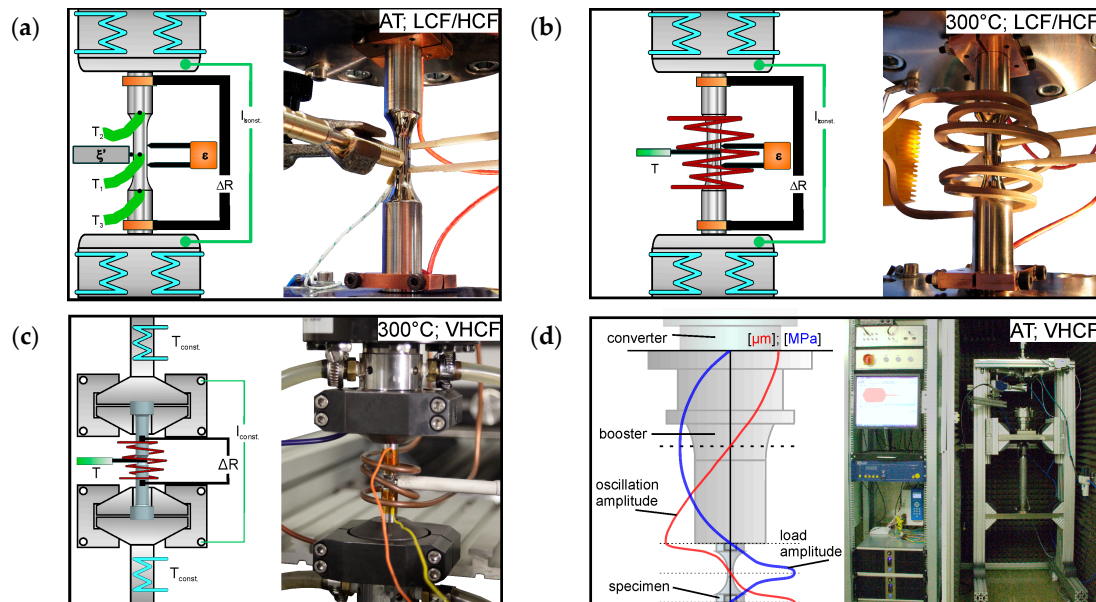


Figure 3. Schematic representation of the experimental setup for fatigue tests in the LCF and HCF regime at (a) AT and (b) at $T = 300\text{ °C}$, as well as in the VHCF regime at (c) $T = 300\text{ °C}$ and (d) at AT.

VHCF testing of metastable austenitic stainless steels at ambient temperature using an ultrasonic fatigue system is more challenging than for stable metallic materials because of transient material behavior and significant self-heating of specimens. Due to the formation of high strength α' -martensite in softer austenite, less damping of the oscillation amplitude takes place, resulting in higher displacement amplitude. Therefore, an unstable displacement amplitude occurred. A representative pulse sequence from the VHCF fatigue test on a fully austenitic microstructure in its initial state and after cyclic loading up to $N \sim 2 \times 10^6$ clearly shows the challenge in performing the fatigue test with constant load amplitude (Figure 4). The first pulses were characterized by an oscillation plateau with a constant amplitude level during each pulse (Figure 4a). These results underline the necessity of a correct specimen design using FEM simulation to ensure fully reversed loading conditions with the maximum stress amplitude in the center of the gauge length and the maximum oscillation amplitude at the specimen's end (see Figure 3d) [65]. However, due to fatigue-induced α' -martensite formation, the initial amplitude plateaus changed to pulses with an increasing displacement level (Figure 4b). This had to be leveled out by appropriate parameter adjustments during phase transformation. Further details can be found in further papers (see [65,69]).

Besides adjusting the proportional, integral and derivative (PID) parameters during VHCF tests, the deformation-induced specimen temperature increase has to be limited. Figure 5a shows the development of displacement for a pulse/pause ratio of 0.5 s/2.5 s, which is typically used for stable metallic materials [64], and which results in an effective load frequency $f_{\text{eff}} = 3300\text{ Hz}$. The progress of the specimen's temperature is also plotted (Figure 5). It can be clearly seen that a pulse/pause ratio of 0.5 s/2.5 s cannot be used for fatigue testing of metastable austenite at ambient temperature because within two pulses the temperature increased to 200 °C (Figure 5a). To keep the specimen's temperature below 50 °C , a change of temperature below 25 K and therefore a pulse/pause ratio of 0.06 s/2.94 s had to be used (Figure 5b). This led to an effective frequency of $f_{\text{eff}} = 400\text{ Hz}$. Theoretically, to achieve the limit of the number of cycles $N_1 = 2 \times 10^9$ for a fatigue test with $f_{\text{eff}} = 400\text{ Hz}$, about 58 days would be required. In reality, with the development of α' -martensite, cyclic hardening of materials takes

place, which reduces cyclic plasticity. Consequently, the development of the specimen's temperature decreases, and fatigue testing could be performed with a higher pulse/pause ratio with $f_{\text{eff}} = 1650$ Hz. The adjustment of PID parameters was also less critical given that saturation of α' -martensite was achieved in the cycle regime of $N \sim 10^8$ (see Figure 10).

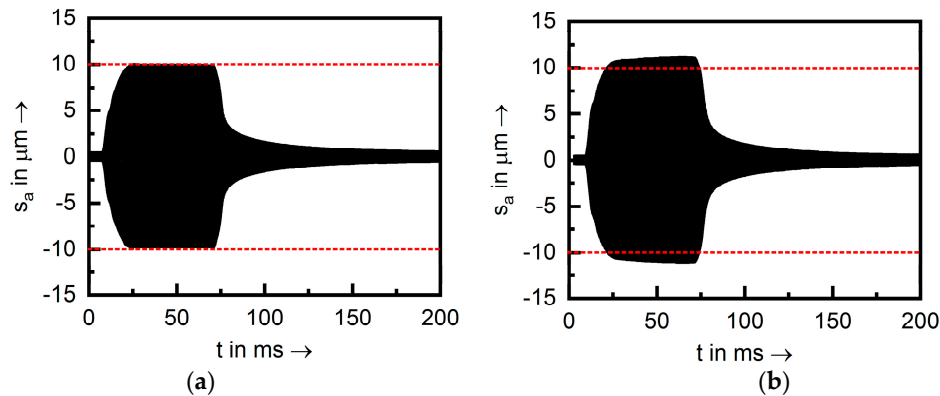


Figure 4. Displacement amplitude of batch A during VHCF testing at (a) the beginning of the fatigue test and (b) after fatigue-induced α' -martensite formation occurred without parameter adjustments.

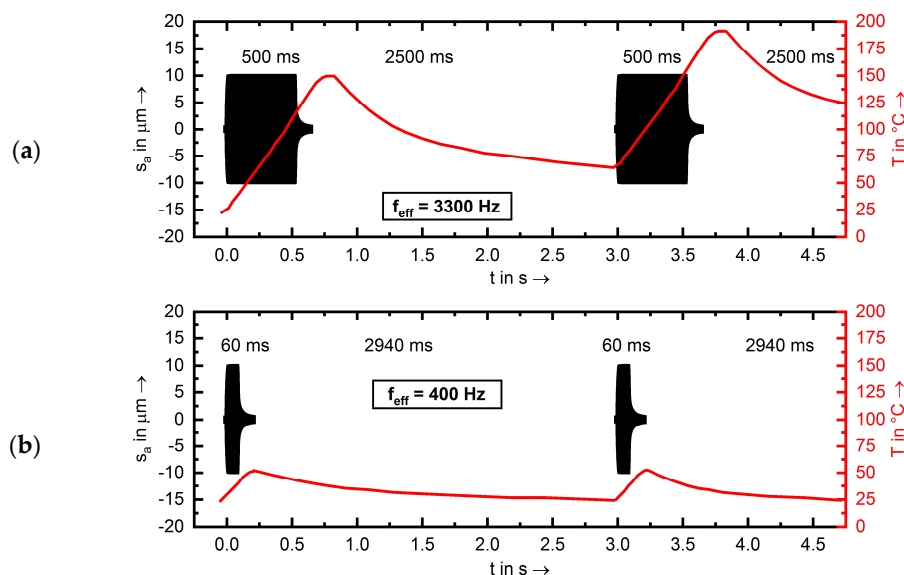


Figure 5. Development of the specimen's temperature using a pulse/pause ratio of (a) 0.5 s/2.5 s and (b) 0.06 s/2.94 s for AISI 347 batch A.

4. Results

Fatigue tests were performed with specimens from AISI 347 batch A taken from an original surge line pipe. Specimens from rolled bars from AISI 347 batch B represented the more metastable material and were used for selected fatigue tests to show the influence of metastability on the deformation and phase transformation behavior in the LCF regime as well as for characterizing HCF behavior at ambient temperature.

4.1. LCF Behavior

4.1.1. Ambient Temperature

Single step (constant amplitude) tests under total-strain control were performed in the LCF regime with total strain amplitudes $0.6\% \leq \varepsilon_{a,t} \leq 1.6\%$, load frequency $f = 0.01$ Hz and triangular waveform. Figure 6 presents the development of stress amplitude (σ_a), the change in specimen

temperature (ΔT) and α' -martensite formation (ξ) for batch A and, additionally, the results from the test with total strain amplitude $\varepsilon_{a,t} = 1.0\%$ for batch B. The cyclic deformation behavior of the investigated steel at ambient temperature was fundamentally determined by deformation-induced austenite- α' -martensite transformation. After a load-dependent number of cycles N , the formation of α' -martensite started and increased continuously with increasing cycle number until specimen failure (Figure 6c). The σ_a - N -curves (Figure 6a) illustrate the associated cyclic hardening processes, which led to a maximum stress amplitude for $\varepsilon_{a,t} \geq 1.2\%$ in the range of the tensile strength $\sigma_f = 569$ MPa (batch A) of the solution-annealed material. Cyclic hardening was detected by temperature measurement, temperature increases in total-strain controlled fatigue tests being indicative of increases of plastic strain energy. Because of very low load frequency, the maximal change in the specimen temperature was below 3 K, which corresponds with an absolute temperature of about 28 °C and consequently bears no significant influence on the formation of α' -martensite. Figure 6c shows the development of α' -martensite content during the fatigue tests discussed above. After an incubation period, which depended on the total strain amplitude, the α' -martensite volume fraction increased continuously with the number of cycles. With increasing $\varepsilon_{a,t}$, the onset of α' -martensite formation was shifted to lower N , and a higher volume fraction of α' -martensite was measured at specimen failure. To characterize the influence of metastability of nominally the same type of austenitic stainless AISI 347 steel, specimens from batches B were cyclically loaded with total strain amplitude $\varepsilon_{a,t} = 1\%$. Both batches A and B showed a continuous cyclic hardening, however, with different gradients after the first ten cycles. In the cycle range $10 < N < 100$, batch A showed only a slight increase of stress amplitude, while batch B underwent a larger increase of σ_a , which correlated directly with a significant development of α' -martensite (Figure 6c) from 1 FE% to 41 FE%. As mentioned in the methods section above, ferromagnetic α' -martensite was measured in situ during fatigue testing using a FeritscopeTM sensor, for which readings above 60 FE% could be inaccurate due to lack in instrument linearity and calibration difficulties at high α' -martensite contents. For this reason, measured data in the range above 60 FE% were plotted as dashed lines in Figure 6c. After a high rate of σ_a increase between $N = 10$ and $N = 100$, batch B showed a decrease in the stress amplitude rate $d\sigma_a/dN$. However, further cyclic hardening took place which led to specimen failure at $\sigma_a = 760$ MPa, which is 120 MPa higher than the tensile strength of this material in its as-received state (Table 2). Batch A also showed evidence of a correlation between the development of α' -martensite and an increase in stress amplitude. However, the start of α' -martensite formation occurred at a higher number of cycles in comparison to batch B and the α' -martensite content was found to be, at the same number of cycles, significantly lower with the maximum value at specimen failure $\xi = 30$ FE%. The results of these tests clearly depicted how substantial the differences can be between the formation of deformation-induced α' -martensite in the same type of austenitic stainless steel due to differences in chemical composition and grain size and consequently the material's metastability. It should be noted that both batches had a chemical composition within the range given in international standards for the investigated steel type.

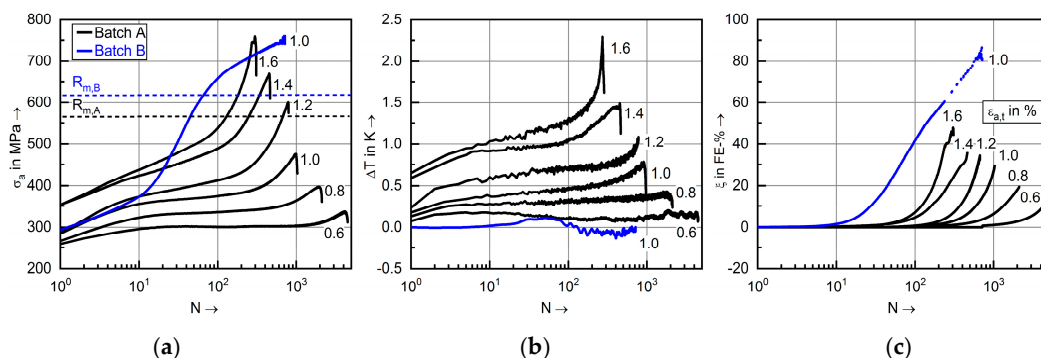


Figure 6. Development of (a) stress amplitude, (b) change in temperature and (c) α' -martensite versus N during total-strain controlled LCF test of batch A and B.

4.1.2. Elevated Temperature $T = 300\text{ }^{\circ}\text{C}$

Single step total-strain control fatigue tests in the LCF regime at $300\text{ }^{\circ}\text{C}$ were performed with total strain amplitudes $0.8\% \leq \varepsilon_{a,t} \leq 1.6\%$, a load frequency $f = 0.01\text{ Hz}$ and triangular waveform. Figure 7 presents the development of the stress amplitude σ_a versus the number of cycles N . At $300\text{ }^{\circ}\text{C}$ the cyclic deformation behavior of the investigated steel was characterized by initial cyclic hardening, followed by slight cyclic softening before the final stress amplitude drop associated with macro crack propagation. The microstructural changes due to cyclic plastic deformation are described elsewhere [46,63]. At these load parameters, no α' -martensite formation occurred and, compared to ambient temperature, the stress amplitude was significantly lower (compared Figure 6a with Figure 7).

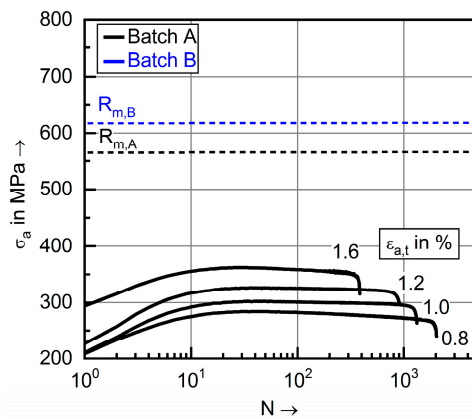


Figure 7. Development of stress amplitude σ_a versus load cycles N during total-strain controlled LCF test at $T = 300\text{ }^{\circ}\text{C}$ of batch A.

4.2. HCF Behavior

For fatigue tests in the HCF regime, stress-controlled single step tests were performed. Typically, in order to obtain the limited number of cycles N_1 in the range of 10^6 – 10^7 cycles, test frequencies in the range $5\text{ Hz} \leq f \leq 20\text{ Hz}$ are used for metallic materials. For $N_1 = 2 \times 10^6$ with a load frequency of $f = 5\text{ Hz}$, about 5 days, for $N_1 = 2 \times 10^7$ with a load frequency $f = 20\text{ Hz}$, about 12 days would be required. Usually, higher test frequencies can be used for HCF tests at ambient temperature (AT) of metallic materials but when investigating the fatigue behavior of metastable austenitic stainless steels, self-heating of the specimens has to be taken into account. Even if external cooling of the specimen is undertaken, significant increases in specimen temperature cannot be suppressed [70,71]. Hence, in this study, test frequencies for fatigue tests at nominally ambient temperature were $f = 5\text{ Hz}$ (batch B) and for $T = 300\text{ }^{\circ}\text{C}$ $f = 20\text{ Hz}$ (batch A).

4.2.1. At Nominally Ambient Temperature

To characterize the cyclic deformation and transformation behavior during cyclic loading in the HCF regime, specimens taken from batch B were cyclically loaded in stress-controlled single step tests with stress amplitudes in the range $225\text{ MPa} \leq \sigma_a \leq 280\text{ MPa}$. In Figure 8a the resulting developments of plastic strain amplitude $\varepsilon_{a,p}$ are plotted against the number of cycles N . The $\varepsilon_{a,p}$, N curves illustrate pronounced cyclic hardening after a short period of initial cyclic softening. Cyclic hardening is caused by an increase in dislocation and stacking fault density, as well as by formation of deformation-induced α' -martensite (Figure 8b). A positive influence of α' -martensite formation on fatigue life was observed, because austenite- α' -martensite transformation causes cyclic hardening, which significantly reduces plastic strain amplitude. Similarly, total-strain controlled fatigue tests in the LCF regime (Figure 6), after an incubation period dependent on stress amplitude, resulted in a continuously increasing volume fraction of α' -martensite over the number of cycles. With increasing stress amplitude, the onset of α' -martensite formation was shifted to lower N and higher α' -martensite fractions were measured at

specimen failure. This development of α' -martensite in stress-controlled tests was comparable to the results given in [16] as well as for total-strain controlled fatigue tests shown in Figure 6c. However, with $1.7 \text{ FE}\% < \xi < 8.8 \text{ FE}\%$ the maximum values of α' -martensite at specimen failure/ultimate number of cycles were significantly lower compared to total strain-controlled LCF tests. The change in the specimen temperature during the fatigue tests is shown in Figure 8c. As in the LCF tests, changes in temperature were used to detect cyclic deformation behavior. However, in the stress-controlled fatigue tests, an increase in temperature correlated with an increase of the σ - ε hysteresis loop area, indicating cyclic softening, whereas a decrease in temperature correlated with a decrease of the σ - ε hysteresis loop area, and characterized cyclic hardening. Besides using ΔT to characterize cyclic deformation behavior, information about the general amount of self-heating is provided (Figure 8c). In consideration of Equation (4), a maximum specimen temperature of $102 \text{ }^\circ\text{C}$ was achieved while the value of ΔT signal shows 53 K. As is known, temperature has a significant influence on deformation-induced α' -martensite formation and consequently fatigue life. In literature [5,72–79] the fatigue life of metastable austenitic stainless steels is given as S-N curves obtained by fatigue testing with load frequencies up to 150 Hz. Obviously, specimen temperatures in HCF tests with frequency higher as 2 Hz were higher than ambient temperature; however, the information about the specimen temperatures is not at all times given. To obtain HCF results at true AT or at temperatures around $25 \text{ }^\circ\text{C}$ – $30 \text{ }^\circ\text{C}$, fatigue tests with significantly lower frequency, e.g. $f = 0.2 \text{ Hz}$, have to be performed. This requires 115 days of test duration to achieve $N_L = 2 \times 10^6$, i.e. a duration that is impractical for systematic investigation of HCF behavior due to high resource expenses. In conclusion, to obtain representative results in the HCF regime in a reasonable time, it is necessary to perform fatigue tests of metastable austenite with variable test frequencies during single step fatigue tests, which effectively suppress self-heating of e.g. $\Delta T_{\text{max}} < 10 \text{ K}$. Therefore, it has to be noted that the presented results (and many others given in literature [5,72–79], especially regarding the development of α' -martensite and its influence on fatigue life) are influenced by specimen temperature, which needs to be taken into consideration.

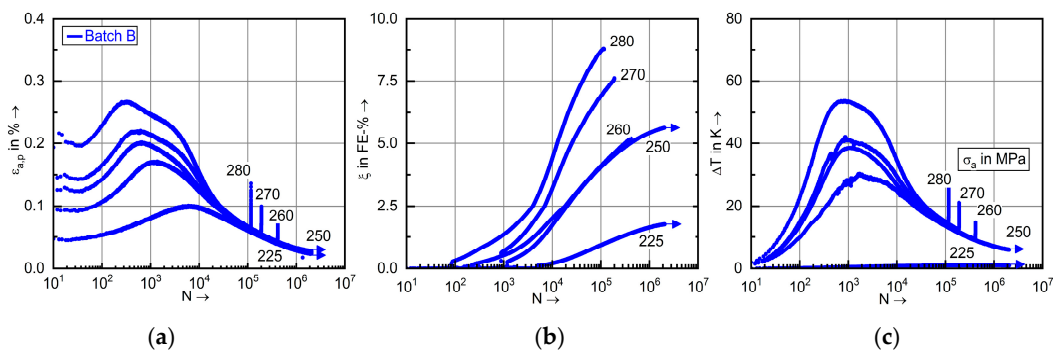


Figure 8. Development of (a) plastic strain amplitude $\varepsilon_{a,p}$, (b) α' -martensite and (c) change in the specimen's temperature ΔT versus load cycles N during HCF tests at AT with $f = 5 \text{ Hz}$ of batch B.

4.2.2. Elevated Temperature $T = 300 \text{ }^\circ\text{C}$

Figure 9 shows the development of plastic strain amplitude during fatigue loading of HCF specimens from batch A at $300 \text{ }^\circ\text{C}$ with a frequency $f = 20 \text{ Hz}$. As these fatigue tests were performed at elevated temperature, a higher test frequency can be used to achieve a reasonable short testing time. At the beginning of the fatigue tests, cyclic softening was detected for all stress amplitudes followed by a saturation state for stress amplitudes $165 \text{ MPa} \leq \sigma_a \leq 200 \text{ MPa}$ and finally crack growth up to specimen failure. Inversely, the stress amplitude of 160 MPa , after initial softening up to about 2×10^4 cycles, led to cyclic hardening, which reduced plastic strain amplitude down to zero. Consequently, macroscopic elastic cyclic loading occurred and at this stress amplitude the limit number of cycles $N_L = 2 \times 10^7$ was achieved without failure. Ex situ magnetic Feritscope™ measurements quantified $0.13 \text{ FE}\%$ for this specimen and $0.00 \text{ FE}\%$ for all loadings $> 160 \text{ MPa}$. That is, for only a small load amplitude at $300 \text{ }^\circ\text{C}$, a change in the cyclic deformation behavior occurred from softening/saturation to cyclic hardening.

This change in cyclic deformation character was also observed during total strain-controlled fatigue tests and detected in situ using electromagnetic induced ultrasonic signals in the specimen [46,47,63]. At 300 °C, the investigated batch A showed no α' -martensite formation during monotonic tensile loading (see Table 2) as well as in LCF [46,47,63] and HCF regimes at “higher” loading amplitudes (see Figures 7 and 9). As mentioned in the introduction, the cyclic deformation behavior of metastable austenitic steels depends on load parameters such as stress amplitude, frequency, and temperature, and results in different microstructural changes from planar dislocation slip, over wavy slip, until the development of stacking faults, twins, as well as ϵ and α' -martensite (see. Figure 1). As the volume fraction of α' -martensite measured by Feritscope™ is relatively low ($\xi = 0.13$ FE%) further microstructural changes have to play a role in the cyclic hardening of metastable austenitic steel at low stress amplitude in fatigue testing at 300 °C, which are still not entirely investigated and explained.

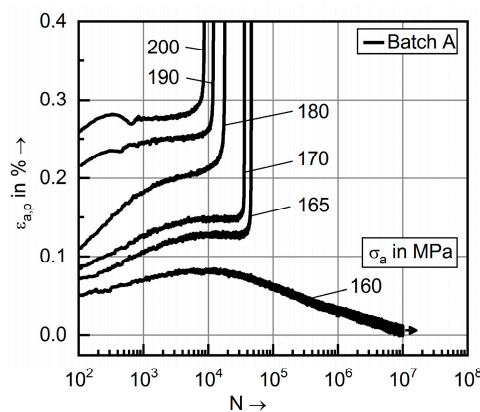


Figure 9. Development of plastic strain amplitude $\epsilon_{a,p}$ versus load cycles N in HCF tests at $T = 300$ °C with $f = 20$ Hz.

4.3. VHCF Behavior

VHCF behavior was investigated at AT using an ultrasonic fatigue system (Figure 3d) at stress amplitudes $180 \text{ MPa} \leq \sigma_a \leq 283 \text{ MPa}$, and a load frequency $f = 20$ kHz, while at $T = 300$ °C a servohydraulic test system was used and stress amplitudes $120 \text{ MPa} \leq \sigma_a \leq 190 \text{ MPa}$ were applied at a load frequency $f = 980$ Hz. All VHCF tests were performed on specimens from batch A.

4.3.1. Ambient Temperature

As σ - ϵ hysteresis measurements are (to date) not realizable during ultrasonic fatigue testing, and due to the macroscopically elastic behavior in the lower HCF/VHCF regime, the cyclic deformation behavior cannot be characterized using conventional data like $\epsilon_{a,p}$, N curves. However, in situ measurement of further physical data, such as changes in the specimen temperature before and after a pulse sequence, dissipated energy and generator power, as well as “quasi in situ” measurement of magnetic properties, can be used to describe the cyclic deformation and transformation behavior of metastable austenites during fatigue testing in the VHCF regime. Figure 10 shows the aforementioned data and, in addition, the displacement amplitude as well as load frequency during an ultrasonic fatigue test with a stress amplitude of 250 MPa. After an approximately stationary phase up to $N = 10^6$, cyclic hardening occurred which could be detected by a strong increase in α' -martensite content. As mentioned before, and illustrated in Figure 4, α' -martensite formation promotes transient material behavior. To keep the displacement amplitude close to a constant value of 9.5 μm , corresponding to a stress amplitude of 250 MPa, the PID parameters of the ultrasonic testing system were stepwise readjusted. The cyclic hardening of the material resulted in lower self-heating illustrated by a decreasing change in temperature. This aspect enabled longer pulse and shorter pause times which resulted in a higher effective frequency. As described in Section 3, a stepwise increase of the pulse pause ratio up to 0.72 s/0.8 s, which represents an effective frequency $f_{\text{eff}} = 1650$ Hz, led to achieving the ultimate number

of cycles within 25 days. After $N = 1 \times 10^8$ load cycles, a lower α' -martensite formation rate $d\xi/dN$ occurred and until the limiting number of cycles a saturation state with a stabilized α' -martensite content of $\xi = 2.2$ FE% was reached. At the same time, temperature as well as displacement amplitude remained constant. In this phase, further adjustments of the displacement control were not necessary. The S-N curve resulting from single step tests is given in Figure 12c. Cyclic plastic deformation of metastable austenite at ambient temperature led to significant changes in phase distribution from single-phase austenitic to two-phase austenite/ α' -martensite microstructures. At ambient temperature, and at all load amplitudes $\sigma_a > 240$ MPa, formation of α' -martensite in the range $0.3 \text{ FE}\% \leq \xi \leq 2.3 \text{ FE}\%$ took place. However, at smaller stress amplitudes $\sigma_a < 240$ MPa no deformation induced α' -martensite was measured. Fatigue failure only occurred in the HCF regime and no specimen failed in the VHCF regime beyond $N = 10^7$ load cycles. Accordingly, a true fatigue limit exists for metastable austenite [80,81].

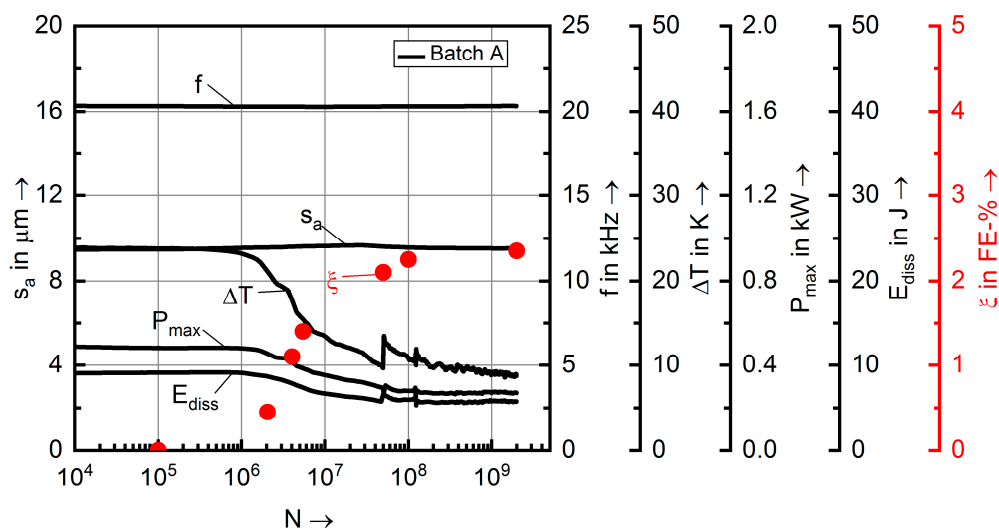


Figure 10. Displacement amplitude s_a , frequency f , temperature change ΔT , power P , dissipated energy E_{dis} and α' -martensite content ξ of batch A during VHCF test at $\sigma_a = 250$ MPa.

4.3.2. Elevated Temperature $T = 300$ °C

High precision stress-strain hysteresis measurement suitable to quantify microplastic deformations at low load amplitudes is, as with ultrasonic fatigue, impossible for tests using servohydraulic systems with a load frequency $f = 980$ Hz. The S-N Woehler curve resulting from constant amplitude fatigue tests at this frequency at 300 °C is given in Figure 12c. Similar to the HCF behavior at 300 °C at low stress amplitude, a very low volume fraction of α' -martensite was detected in the specimen which achieved the limit number of cycles $N_1 = 5 \times 10^8$. Since the FerritscopeTM sensor cannot be used in situ at this testing temperature, the kinetics of α' -martensite development was analyzed by an interrupted VHCF test with a stress amplitude of 160 MPa. At defined load cycles, ex situ FerritscopeTM measurements were taken at the specimen surface at ambient temperature. Figure 11 shows no α' -martensite up to $N = 1 \times 10^7$. The onset of α' -martensite formation occurred between $N = 1 \times 10^7$ and $N = 1 \times 10^8$. At $N = 1 \times 10^8$ 0.12 FE% and at $N = 5 \times 10^8$ 0.13 FE% were measured without specimen failure. As the measured volume fraction of α' -martensite was very low, further microstructural changes had to play a role in the cyclic hardening of metastable austenitic steel in the VHCF regime at 300 °C.

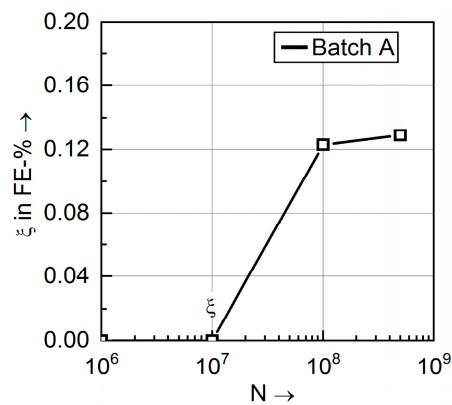


Figure 11. Development of α' -martensite during the interrupted VHCF test at $\sigma_a = 160$ MPa, $f = 980$ Hz and $T = 300$ °C.

5. Summary

Figure 12 summarizes the results from fatigue tests on AISI 347 in LCF, HCF and VHCF regimes at AT and 300 °C in the form of S-N curves. The influences of metastability of two different batches of AISI 347 on cyclic deformation behavior are clearly seen in LCF tests at ambient temperature (see Figure 6). The determined total strain-controlled fatigue life in the LCF regime at AT and 300 °C is similar (Figure 12a). However, significantly different cyclic deformation behavior was observed. At AT, cyclic hardening due to α' -martensite formation took place and the transformation from a single-phase austenitic to two-phase austenite/ α' -martensite microstructure developed. The results epitomize a “dynamical composite material” with changing volume fraction and distribution of “reinforcements” during cyclic loading. At 300 °C in the LCF regime, no α' -martensite was measured and cyclic deformation behavior showed slight initial cyclic hardening followed by saturation/softening. Despite significantly different cyclic deformation behavior and resulting stress amplitudes in AT and $T = 300$ °C, respectively, similar fatigue lifetimes were estimated. However, the specimens loaded at AT achieved stresses higher than the ultimate tensile strength. A positive influence of α' -martensite formation on fatigue life was observed in stress-controlled fatigue tests in the HCF regime (Figure 12b) where austenite- α' -martensite transformation caused hardening, which significantly reduced the plastic strain amplitude and led to increased fatigue life. The α' -martensite formation occurred in all fatigue tests at AT. At 300 °C, albeit specimens loaded with low stress amplitude showed a very small volume fraction of α' -martensite. These specimens achieved the limit number of cycles without failure. A comparison of the S-N curves from tests at AT with $T = 300$ °C clearly showed a decrease in fatigue strength with an increase of temperature (Figure 12b). Similar behavior was observed for VHCF tests at AT and 300 °C (Figure 12c). At AT, higher fatigue strength existed, which correlated with the development of α' -martensite at each load amplitude. At 300 °C, only specimens with the formation of a low volume fraction of α' -martensite achieved the limit of the number of cycles without failure.

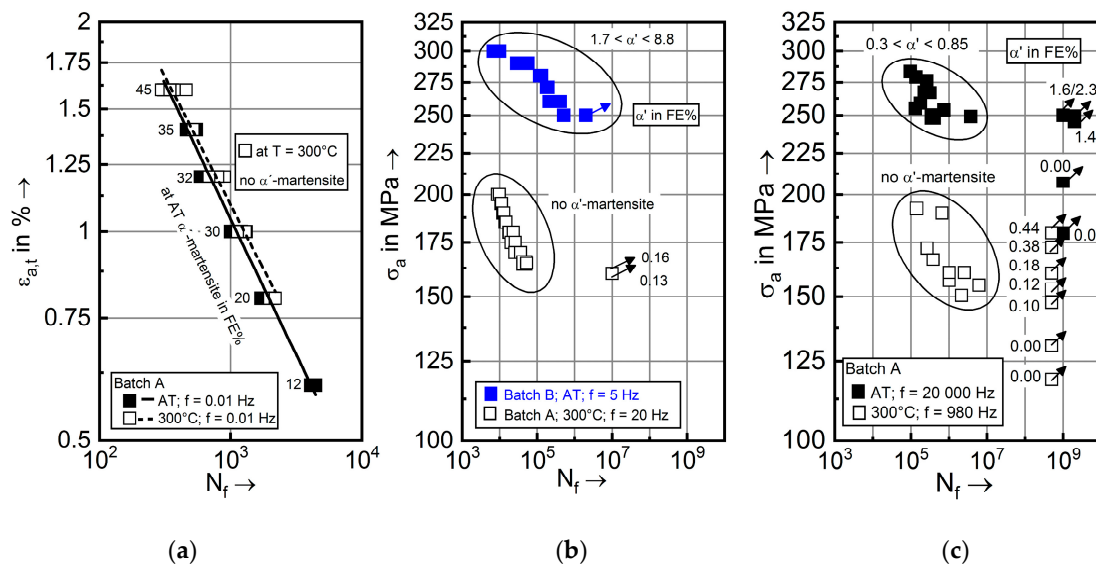


Figure 12. (a) $\varepsilon_{a,t}$ - N curve in LCF regime of batch A at AT and $T = 300^\circ\text{C}$, (b) S- N curve in HCF regime of batch A at $T = 300^\circ\text{C}$ and batch B at AT, (c) S- N curve in VHCF regime of batch A at AT and $T = 300^\circ\text{C}$.

6. Conclusions

The present study characterized fatigue behavior of metastable austenitic stainless steels in the LCF, HCF and VHCF regimes at two temperatures, i.e. ambient temperature and 300°C . Based on the acquired results, the following conclusions were drawn:

- The metastability of austenitic Cr-Ni steels can, even within the specifications given in international standards, e.g. for AISI 347 stainless steel, strongly vary due to relatively small changes in chemical composition.
- Different metastability of austenitic stainless steel affects the cyclic deformation and, consequently, the fatigue lifetime behavior.
- This is caused by the fact that during fatigue, various deformation (planar or wavy slip character, formation of stacking faults, twinning) and transformation ($\gamma \rightarrow \varepsilon$, $\gamma \rightarrow \varepsilon \rightarrow \alpha'$, $\gamma \rightarrow \alpha'$) mechanisms with different peculiarity take place.
- The investigated metastable austenitic stainless steel AISI 347 showed a true fatigue limit in the VHCF regime at AT and 300°C .
- Further microstructural investigations have to be performed with focus on the development of deformation/transformation mechanism maps dependent on metastability parameters, e.g. stacking fault energy and loading parameters, in the LCF, HCF and VHCF regimes in accordance with deformation maps known in the literature [52–54] for stable materials.

Author Contributions: M.S. planned the experimental design and wrote the majority of the present paper; A.B., T.D., R.S. and A.S. realized experimental investigations and analysis of the given results; M.S. and T.B. supervision the work.

Funding: This research was funded by Federal Ministry for Economic Affairs and Energy (BMWi), Germany and the German Research Foundation (DFG).

Acknowledgments: The authors thank BMWi as well as the DFG for financial support as part of the CRC 926 project number 172116086 “Microscale Morphology of Component Surfaces”.

Conflicts of Interest: The authors declare no conflict of interest.

References

1. Strauß, B.; Maurer, E. Die hochlegierten Chrom-Nickel-Stähle als nichtrostende Stähle. *Kruppsche Monatshefte* **1920**, *1*, 129–146.
2. Lo, K.H.; Shek, C.H.; Lai, J.K.L. Recent developments in stainless steels. *Mater. Sci. Eng.* **2009**, *R65*, 39–104. [[CrossRef](#)]
3. Leuk Lai, J.K.; Lo, K.H.; Shek, C.H. *Stainless Steels: An Introduction and Their Recent Developments*; Bentham Science Publishers: Sharjah, United Arab Emirates, 2012.
4. Marshall, P. *Austenitic stainless steels: Microstructure and Mechanical Properties*. Springer Science & Business Media: Berlin, Germany, 1984.
5. Chopra, O.K.; Shack, W.J. Effect of LWR coolant environments on the fatigue life of reactor materials. In *Final Report, NUREG/CR-6909*; Argon National Laboratory: Lemont, IL, USA, 2007.
6. Deutsche Edelstahlwerke Rost-, säure- und hitzebeständige Stähle. 2010. Available online: https://www.dew-stahl.com/fileadmin/files/dew-stahl.com/documents/Publikationen/Broschueren/014_DEW_RSH_D.pdf (accessed on 30 May 2019).
7. Hull, F.C. Delta ferrite and martensite formation in stainless steels. *Weld. J. Res. Suppl.* **1973**, *179*, 193–203.
8. Padilha, A.F.; Martorano, M.A. Predicting delta ferrite content in stainless steel castings. *ISIJ INT* **2012**, *52*, 1054–1065.
9. Padilha, A.F.; Tavares, C.F.; Martorano, M.A. Delta ferrite formation in austenitic stainless steel castings. *Mater. Sci. Forum* **2013**, *730–732*, 733–738. [[CrossRef](#)]
10. Graham, C.D.; Loren, B.E. Delta ferrite is ubiquitous in type 304 stainless steel: Consequences for magnetic characterization. *J. Magn. Magn. Mater.* **2018**, *458*, 15–18. [[CrossRef](#)]
11. Schäffler, A.L. Constitution diagram for stainless steel weld metal. *Met. Prog.* **1949**, *56*, 608–680B.
12. Becker, H.; Brandis, H.; Küppers, W. Zur Verfestigung instabil austenitischer nichtrostender Stähle und ihre Auswirkung auf das Umformverhalten von Feinblechen. *Thyssen Edelst. Techn. Berichte* **1986**, *12*, 35–54.
13. Eichelman, G.H.; Hull, F.C. The effect of composition in the temperature of spontaneous transformation of austenite to martensite in 18-8 type stainless steel. *Trans. ASM* **1952**, *45*, 77–104.
14. Angel, T. Formation of martensite in austenitic stainless steels—Effects of deformation, temperature and composition. *J. Iron. Steel Inst.* **1954**, *177*, 165–174.
15. Man, J.; Smaga, M.; Kuběna, I.; Eifler, D.; Polák, J. Effect of metallurgical variables on the austenite stability in fatigued AISI 304 type steels. *Eng. Fract. Mech.* **2017**, *185*, 139–159. [[CrossRef](#)]
16. Smaga, M.; Boemke, A.; Daniel, T.; Klein, M.W. Metastability and fatigue behavior of austenitic stainless steels. *MATEC Web Conf.* **2018**, *165*, 04010. [[CrossRef](#)]
17. Olson, G.B.; Cohen, M. A general mechanism of martensitic nucleation: Part I. General concepts and the FCC \rightarrow HCP transformation. *Metall. Trans. A* **1976**, *7*, 1897–1904.
18. Olson, G.B.; Cohen, M. A general mechanism of martensitic nucleation: Part II. General concepts and the FCC \rightarrow HCP transformation. *Metall. Trans. A* **1976**, *7*, 1905–1914.
19. Olson, G.B.; Cohen, M. A general mechanism of martensitic nucleation: Part III. General concepts and the FCC \rightarrow HCP transformation. *Metall. Trans. A* **1976**, *7*, 1915–1923. [[CrossRef](#)]
20. Schumann, H. Verformungsinduzierte Martensitbildung in metastabilen austenitischen Stählen. *Krist. Tech.* **1975**, *10*, 401–411. [[CrossRef](#)]
21. Sinclair, C.W.; Hoagland, R.G. A molecular dynamics study of the fcc \rightarrow bcc transformation at fault intersections. *Acta Mater.* **2008**, *56*, 4160–4171. [[CrossRef](#)]
22. Shimizu, K.; Tanaka, Y. The $\gamma \rightarrow \epsilon \rightarrow \alpha'$ martensitic transformations in an Fe–Mn–C Alloy. *Trans. Jpn. Inst. Met.* **1978**, *19*, 685–693. [[CrossRef](#)]
23. Spencer, K.; Embury, J.D.; Conlon, K.T.; Véron, M.; Bréchet, Y. Strengthening via the formation of strain-induced martensite in stainless steels. *Mater. Sci. Eng. A* **2004**, *387–389*, 873–881. [[CrossRef](#)]
24. Venables, J.A. Martensite transformation in stainless steels. *Philos. Mag.* **1962**, *7*, 35–44. [[CrossRef](#)]
25. Scheil, E. Über die Umwandlung des Austenits in Martensit in Eisen-Nickellegierungen unter Belastung. *Z. Anorg. Allg. Chem.* **1932**, *207*, 21–40. [[CrossRef](#)]
26. Smaga, M.; Eifler, D. Fatigue life calculation of metastable austenitic stainless steels on the basis of magnetic measurements. *Mater. Test.* **2009**, *51*, 370–375. [[CrossRef](#)]

27. Biermann, H.; Solarek, J.; Weidner, A. SEM Investigation of High-Alloyed Austenitic Stainless Cast Steels With Varying Austenite Stability at Room Temperature and 100 degrees C. *Steel Res. Int.* **2012**, *83*, 512–520. [[CrossRef](#)]
28. Hahnenberger, F.; Smaga, M.; Eifler, D. Influence of γ - α' -phase transformation in metastable austenitic steels on the mechanical behavior during tensile and fatigue loading at ambient and lower temperatures. *Adv. Eng. Mater.* **2012**, *14*, 853–858. [[CrossRef](#)]
29. Hahnenberger, F.; Smaga, M.; Eifler, D. Microstructural investigation of the fatigue behavior and phase transformation in metastable austenitic steels at ambient and lower temperatures. *Int J. Fatigue* **2014**, *69*, 36–48. [[CrossRef](#)]
30. Smaga, M.; Hahnenberger, F.; Sorich, A.; Eifler, D. Cyclic deformation behavior of austenitic steels in the temperature range $-60\text{ C} \leq T \leq 550\text{ }^\circ\text{C}$. *Key Eng. Mater.* **2011**, *465*, 439–442. [[CrossRef](#)]
31. Curtze, S.; Kuokkala, V.T.; Oikari, A.; Talonen, J.; Hänninen, H. Thermodynamic modeling of the stacking fault energy of austenitic steels. *Acta Mater.* **2011**, *59*, 1068–1076. [[CrossRef](#)]
32. Jun, J.H.; Choi, C.-S. Variation of stacking fault energy with austenite grain size and its effect on the M_5 temperature of $\gamma \rightarrow \epsilon$ martensitic transformation in Fe–Mn alloy. *Mater. Sci. Eng. A* **1998**, *257*, 353–356. [[CrossRef](#)]
33. Llewellyn, D.T. Work hardening effects in austenitic stainless steels. *Mater. Sci. Technol.* **1997**, *13*, 389–400. [[CrossRef](#)]
34. Martin, S.; Fabrichnaya, O.; Rafaja, D. Prediction of the local deformation mechanisms in metastable austenitic steels from the local concentration of the main alloying elements. *Mater. Lett.* **2015**, *159*, 484–488. [[CrossRef](#)]
35. Otte, H.M. The transformation of stacking faults in austenite and its relation to martensite. *Acta Metall.* **1957**, *5*, 614–627. [[CrossRef](#)]
36. Rhodes, C.G.; Thompson, A.W. The composition dependence of stacking fault energy in austenitic stainless steels. *Metall. Mater. Trans. A* **1977**, *8*, 1901–1906. [[CrossRef](#)]
37. Rémy, L.; Pineau, A.; Thomas, B. Temperature dependence of stacking fault energy in close-packed metals and alloys. *Mater. Sci. Eng.* **1978**, *36*, 47–63. [[CrossRef](#)]
38. Shen, Y.F.; Li, X.X.; Sun, X.; Wang, Y.D.; Zuo, L. Twinning and martensite in a 304 austenitic stainless steel. *Mater. Sci. Eng. A* **2012**, *552*, 514–522. [[CrossRef](#)]
39. Schramm, R.E.; Reed, R.P. Stacking-fault energies of 7 commercial austenitic stainless steels. *Metall. Trans. A* **1975**, *6*, 1345–1351. [[CrossRef](#)]
40. Basu, K.; Das, M.; Bhattacharjee, D.; Chakraborti, P.C. Effect of grain size on austenite stability and room temperature low cycle fatigue behavior of solution annealed AISI 316LN austenitic stainless steel. *Mater. Sci. Technol.* **2007**, *23*, 1278–1284. [[CrossRef](#)]
41. Gonzáles, J.L.; Aranda, R.; Jonapá, M. The influence of grain size on the kinetics of strain induced martensite in type 304 stainless steel. In *Applications of Stainless Steel*; Nordberg, H., Björklund, J., Eds.; ASM International: Stockholm, Sweden, 1992; pp. 1009–1016.
42. Shrinivas, V.; Varma, S.K.; Murr, L.E. Deformation-Induced martensitic characteristics in 304 stainless and 316 stainless steels during room temperature rolling. *Metall. Mater. Trans. A* **1995**, *26*, 661–671. [[CrossRef](#)]
43. Yang, H.S.; Bhadeshia, H.K.D.H. Austenite grain size and the martensite–Start temperature. *Scr. Mater.* **2009**, *60*, 493–495. [[CrossRef](#)]
44. Bayerlein, M.; Christ, H.J.; Mughrabi, H. Plasticity-induced martensitic transformation during cyclic deformation of AISI 304L stainless steel. *Mater. Sci. Eng. A* **1989**, *114*, L11–L16. [[CrossRef](#)]
45. Smaga, M.; Walther, F.; Eifler, D. Deformation-induced martensitic transformation in metastable austenitic steels. *Mater. Sci. Eng. A* **2008**, *483–484*, 394–397. [[CrossRef](#)]
46. Sorich, A.; Smaga, M.; Eifler, D. Fatigue monitoring of austenitic steels with electromagnetic acoustic transducers (EMATs). *Mater. Performance Charact.* **2014**, *4*, 263–274. [[CrossRef](#)]
47. Sorich, A.; Smaga, M.; Eifler, D. Influence of cyclic deformation induced phase transformation on the fatigue behavior of the austenitic steel X6CrNiNb1810. *Adv. Mater. Res.* **2014**, *891–892*, 1231–1236. [[CrossRef](#)]
48. Das, A.; Sivaprasad, S.; Ghosh, M.; Chakraborti, P.C.; Tarafder, S. Morphologies and characteristics of deformation induced martensite during tensile deformation of 304 LN stainless steel. *Mater. Sci. Eng. A* **2008**, *486*, 283–286. [[CrossRef](#)]

49. Murr, L.E.; Staudhammer, K.P.; Hecker, S.S. Effects of strain state and strain rate on deformation-induced transformation in 304 stainless steel: part ii. microstructural study. *Metall. Trans. A* **1982**, *13*, 627–635. [[CrossRef](#)]
50. Staudhammer, K.P.; Murr, L.E.; Hecker, S.S. Nucleation and evolution of strain-induced martensitic (bcc) embryos and substructure in stainless-steel—A transmission electron-microscope study. *Acta Metall.* **1983**, *31*, 267–274. [[CrossRef](#)]
51. Hecker, S.S.; Stout, M.G.; Staudhammer, K.P.; Smith, J.L. Effects of strain state and strain rate on deformation-induced transformation in 304 stainless steel: Part I. Magnetic measurements and mechanical behavior. *Metall. Trans. A* **1982**, *13*, 619–626. [[CrossRef](#)]
52. Klesnil, M.; Lukas, P. Fatigue of metallic materials. *Mater. Sci. Monogr.* **1980**, *7*.
53. Lukáš, P.; Klesnil, M. Dislocation structures in fatigued single crystals of Cu-Zn system. *Phys. Stat. Sol. (a)* **1971**, *5*, 247–258. [[CrossRef](#)]
54. Mughrabi, H. Fatigue, an everlasting materials problem—still en vogue. *Proc. Eng.* **2010**, *2*, 3–26. [[CrossRef](#)]
55. Karaman, I.; Sehitoglu, H.; Chumlyakov, Y.I.; Maier, H.J. The deformation of low-stacking-fault-energy austenitic steels. *JOM* **2002**, *7*, 31–37. [[CrossRef](#)]
56. Lee, T.-H.; Shin, E.; Oh, C.-S.; Ha, H.-Y.; Kim, S.-J. Correlation between stacking fault energy and deformation microstructure in high-interstitial-alloyed austenitic steels. *Acta Mater.* **2010**, *58*, 3173–3186. [[CrossRef](#)]
57. Xie, X.; Ninga, D.; Suna, J. Strain-controlled fatigue behavior of cold-drawn type 316 austenitic stainless steel at room temperature. *Mater. Charact.* **2016**, *120*, 195–202. [[CrossRef](#)]
58. Nebel, T. Verformungsverhalten und Mikrostruktur zyklisch beanspruchter metastabiler austenitischer Stähle. Ph.D. Thesis, Technical University of Kaiserslautern, Kaiserslautern, Germany, September 2002.
59. Bassler, H.J. Wechselverformungsverhalten und verformungsinduzierte Martensitbildung bei dem metastabilen austenitischen Stahl X6CrNiTi1810. Ph.D. Thesis, Technical University of Kaiserslautern, Kaiserslautern, Germany, December 1999.
60. *German version EN 10088-1:2014 Stainless steels – Part 1: List of stainless steels*; DIN Deutsches Institut für Normung e. V.: Berlin, Germany, 2014.
61. Ausschuss, K. *Sicherheitstechnische Regel des KTA – KTA 3204 Reaktordruckbehälter-Einbauten*; Carl Heymanns Verlag: Cologne, Germany, 2015.
62. Smaga, M.; Sorich, A.; Eifler, D.; Beck, T. Very high cycle fatigue behavior of metastable austenitic steel X6CrNi1810 at 300 °C. In Proceedings of the 7th International Conference on Very High Cycle Fatigue (VHCF-7), Dresden, Germany, 3–5 July 2017.
63. Sorich, A. Charakterisierung des Verformungs- und Umwandlungsverhaltens des zyklisch beanspruchten metastabilen austenitischen Stahls X6CrNiNb1810. Ph.D. Thesis, Technical University of Kaiserslautern, Kaiserslautern, Germany, July 2006.
64. Ritz, F.; Beck, T. Influence of mean stress and notches on the very high cycle fatigue behavior and crack initiation of a low-pressure steam turbine steel. *Fatigue Fract. Eng. Mater. Struct.* **2017**, *40*, 1762–1771. [[CrossRef](#)]
65. Daniel, T.; Boemke, A.; Smaga, M.; Beck, T. Investigations of very high cycle fatigue behavior of metastable austenitic steels using servohydraulic and ultrasonic testing systems. In Proceedings of the ASME 2018 Pressure Vessels and Piping Conference, Prague, Czech Republic, 15–20 July 2018.
66. Biallas, G.; Piotrowski, A.; Eifler, D. Cyclic stress-strain, stress-temperature and stress-electrical resistance response of NiCuMo alloyed sintered steel. *Fatigue Fract. Eng. Mater. Struct.* **1995**, *18*, 605–615. [[CrossRef](#)]
67. Piotrowski, A.; Eifler, D. Characterization of cyclic deformation behaviour by mechanical, thermometrical and electrical methods. *Materialwiss. Werkstofftech.* **1995**, *26*, 121–127.
68. Talonen, J.; Aspegren, P.; Hänninen, H. Comparison of different methods for measuring strain induced alpha ' -martensite content in austenitic steels. *Mater. Sci. Technol.* **2004**, *20*, 1506–1512. [[CrossRef](#)]
69. Boemke, A.; Smaga, M.; Beck, T. Influence of surface morphology on the very high cycle fatigue behavior of metastable and stable austenitic Cr-Ni steels. *MATEC Web Conf.* **2018**, *165*, 20008. [[CrossRef](#)]
70. Nikitin, B.; Besel, M. Effect of low-frequency on fatigue behavior of austenitic steel AISI 304 at room temperature and 25 °C. *Int. J. Fatigue* **2008**, *30*, 2044–2049. [[CrossRef](#)]
71. Pessoa, D.F.; Kirchhoff, G.; Zimmermann, M. Influence of loading frequency and role of surface micro-defects on fatigue behavior of metastable austenitic stainless steel AISI 304. *Int. J. Fatigue* **2017**, *103*, 48–59. [[CrossRef](#)]

72. De Backer, F.; Schoss, V.; Maussner, G. Investigations on the evaluation of the residual fatigue life-time in austenitic stainless steels. *Nucl. Eng. Des.* **2001**, *206*, 201–219. [[CrossRef](#)]
73. Le Duff, J.-A.; Lefrançois, A.; Meyzaud, Y.; Vernot, J.-Ph.; Martin, D.; Mendez, J.; Lehericy, Y. High cycle thermal fatigue issues in PWR nuclear power plants, lifetime improvement of some austenitic stainless steel components. *Metall. Res. Technol.* **2007**, *104*, 156–162.
74. Laamouri, A.; Sidhom, H.; Braham, C. Evaluation of residual stress relaxation and its effect on fatigue strength of AISI 316L stainless steel ground surfaces: Experimental and numerical approaches. *Int J. Fatigue* **2013**, *48*, 109–121. [[CrossRef](#)]
75. Vincent, L.; Le Roux, J.-C.; Taheri, S. On the high cycle fatigue behavior of a type 304L stainless steel at room temperature. *Int. J. Fatigue* **2012**, *38*, 84–91. [[CrossRef](#)]
76. Puchi-Cabrera, E.S.; Staia, M.H.; Tova, C.; Ochoa-Pérez, E.A. High cycle fatigue behavior of 316L stainless steel. *Int. J. Fatigue* **2008**, *30*, 2140–2146. [[CrossRef](#)]
77. Roth, I.; Kübbeler, M.; Krupp, U.; Christ, H.-J.; Fritzen, C.-P. Crack initiation and short crack growth in metastable austenitic stainless steel in the high cycle fatigue regime. *Proc. Eng.* **2010**, *2*, 941–948. [[CrossRef](#)]
78. Soo, P.; Chow, J.G.Y. High cycle fatigue behavior of solution annealed and thermally aged Type 304 stainless steel. *J. Eng. Mater. Technol.* **1980**, *102*, 141–146. [[CrossRef](#)]
79. Herrera-Solaz, V.; Niffenegger, M. Application of hysteresis energy criterion in a microstructure-based model for fatigue crack initiation and evolution in austenitic stainless steel. *Int. J. Fatigue* **2017**, *100*, 84–93. [[CrossRef](#)]
80. Müller-Bollenhagen, C.; Zimmermann, M.; Christ, H.-J. Adjusting the very high cycle fatigue properties of a metastable austenitic stainless steel by means of the martensite content. *Proc. Eng.* **2010**, *2*, 1663–1672. [[CrossRef](#)]
81. Grigorescu, A.; Kolyshkin, A.; Zimmermann, M.; Christ, H.-J. Effect of martensite content and geometry of inclusions on the VHCF properties of predeformed metastable austenitic stainless steels. *Procedia Struct. Integrity* **2016**, *2*, 1093–1100. [[CrossRef](#)]



© 2019 by the authors. Licensee MDPI, Basel, Switzerland. This article is an open access article distributed under the terms and conditions of the Creative Commons Attribution (CC BY) license (<http://creativecommons.org/licenses/by/4.0/>).